Finite Element Analysis of Underwater Wet Welding: The Implementation of Bubble Configuration

An improved simulation of the temperature field in underwater wet welding with modified boundary conditions was proposed

BY J. WANG, Y. Y. CHEN, J. LIU, T. ZHANG, C. LIU, C. YAN, AND Y. C. FENG

Abstract

To reasonably characterize the features of underwater wet welding, especially the bubble effect engendered from a high concentration of heat, a three-dimensional (3D) numerical model considering the interaction of bubble dynamics with the boundary layer was developed. A semi-empirical method assessing the bubble growth process was incorporated into the model as boundary conditions to account for the heat loss mechanism. It was proven that consideration of the bubble configuration can improve prediction accuracy, and the predicted weld profile was in good agreement with the experimental results. To reveal the contribution of the bubble configuration while maintaining processing variables consistency, the influences of the equivalent contact radius of the bubble and its floating frequency on the temperature field evolution were evaluated. The results showed that low floating frequency and/or a high equivalent contact radius tend to depress the heat losses to a water environment, prolong the $t_{8/5}$ time, and enhance the weld width and joint penetration, which render the role of optimized bubble dynamics beneficial. Under otherwise identical conditions, the equivalent contact radius of the bubble plays a much better role than the bubble floating frequency in promoting weld pool dimensions. Based on the quantified data, suggestions concerning the matching strategy of bubble configuration and heat input for underwater wet welding may be provided.

Keywords

- Finite Element Analysis
- Modified Boundary Conditions
- Bubble Dynamics
- Temperature Field
- Underwater Wet Welding

Introduction

Underwater wet welding, a widely applied arc welding method in the construction and maintenance of offshore engineering structures, is characterized by its process simplicity and excellent reliability (Refs. 1–3). Maintained between the electrode and base material, the arc plasma is wrapped in a dry, gaseous environment, which is usually referred to as a bubble, and thereby nominally isolated from water (Refs. 4, 5). The interaction between the bubble, arc plasma, molten droplet, and weld pool is described in Fig. 1. Moving the heat source and the associated bubble cause the molten metal inside the bubble to flow to the rear area, where it resolidifies to create a weld bead (Ref. 6). In addition, bubble configuration is the primary attribute of the underwater wet welding process, which makes the process directly in contact with water and allows repair or construction of the most geometrically complex structures.

Note that the bubble itself exhibits various dynamic behaviors of formation, growth, detachment, rise, and subsequent bursting in the freeboard region (Ref. 7). Therefore, bubble dynamics play an essential role in the degradation of the welding process due to considerable physical interactions taking place between the bubble, arc plasma, molten droplet, and weld pool. The adverse effects of bubble dynamics on the welding process have been extensively investigated. Jia et al. (Refs. 8, 9) explored the relationship between bubble
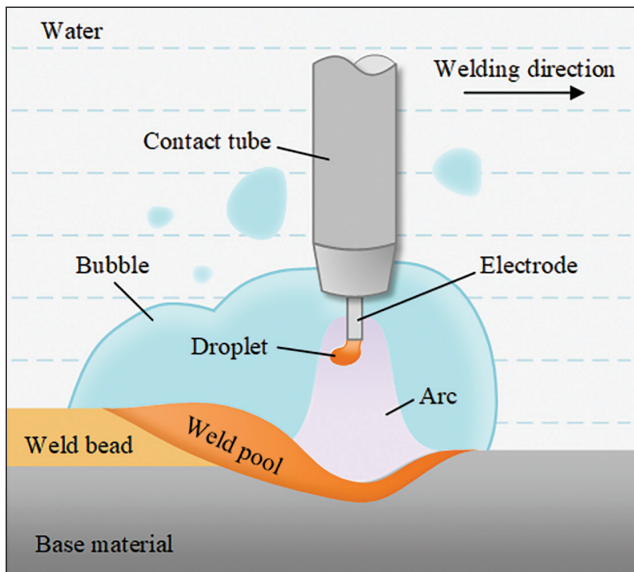
Fig. 1 — Schematic of the bubble-arc-droplet-weld pool zone in underwater wet welding.

oscillation and arc stability and concluded that arc deviation is usually promoted by bubble disturbance. Wang et al. (Refs. 10, 11) performed electrical signal analysis in underwater wet welding and found that the improvement of bubble stability could help realize the control of welding current waveforms. Subsequently, x-ray transmission studies revealed the generation of a repelled transfer mode and reported that gas flow drag force should account for this phenomenon due to variations of bubble volume and motion in a water medium (Ref. 12). As for external conditions, hydrostatic pressure (Ref. 13) and water flow (Refs. 14, 15) are crucial factors in disturbing bubble stability, resulting in the deterioration of the welding process.

On the other hand, Tsai and Masubuchi (Ref. 16) investigated the heat loss mechanisms in underwater wet welding and pointed out that the interaction between cold water and the oscillating bubble should be responsible for rapid cooling. Arias and Bracarense (Ref. 17) and Klett et al. (Ref. 18) concluded that brittle microstructure and cold cracking are governed by the level of cooling rate, which is also attributed to the oscillation of the rising bubble. Thus, the in-situ local heat treatment method (Ref. 19) and the temper bead welding technique (Ref. 20) have been documented since the detrimental microstructure is minimized, but the contribution of bubble oscillation has not been taken into account. In general, underwater wet welding relies on a bubble to achieve a desired weld bead, and the bubble plays a multiplicity of roles during the welding process, such as stabilizing the arc (Ref. 21), promoting metal transfer (Ref. 22), reducing the appearance of spatter (Ref. 23), protecting the weld pool from water contamination (Ref. 24), and regulating heat distribution (Ref. 25). However, the studies reviewed above only considered the role of bubble dynamics on the final welding process, in which the intrinsic properties of bubble dynamics, especially their correlation with the heat loss mechanism, were not probed and evaluated.

Currently, rapid cooling associated with bubble dynamics is an important issue in applying underwater wet welding (Refs. 16, 26). The quality of the weld depends highly on the rapid cooling associated with bubble dynamics, which depends on many factors, especially the physical characteristics of the gas-liquid-solid interface (bubble base) that stays at the weld pool (Ref. 27) and the processing variables to be used (Ref. 28). Hence, rapid cooling associated with bubble dynamics is susceptible to the variation in processing variables, which in turn confers a narrower range of applicable processing variables for an acceptable weld bead. It appears that most of the applicable processing variables tend to require numerous experiments for verification. Ronda et al. (Ref. 29) emphasized that numerical simulation of the temperature field offers an alternative method for assessing the underwater wet welding process and allows optimization of processing variables. Ghadimi et al. (Ref. 30) investigated the temperature profiles, thermal history curves, and cooling rate for single-pass underwater wet weldments by using a 3D finite difference method and observed that convective heat transfer is more effective in temperature calculations than radiation heat transfer. Zhao et al. (Ref. 26) simulated the bubble evolution promoted by an arc plasma and flux decomposition using hydrodynamic equations in underwater wet welding and found that heat transfer to the upper region of the goblet-shaped bubble is one of the high heat-loss mechanisms during the bottom shrinkage stage of the bubble. Pan et al. (Ref. 31) introduced the pool boiling heat transfer theory into the hybrid heat source model and predicted that a lower $t_{8/5}$ value near the fusion zone is expected to cause the formation of fully transformed martensite. Wang et al. (Ref. 32) developed a double-ellipsoid heat source model considering material removal and arc heat and proved that the model and boundary condition in this study are applicable to underwater arc cutting.

However, the numerical simulation studies reported above often overlooked the action of bubble dynamics on the thermal properties so that it was not faithfully reflected in the welding process (Ref. 33). The bubble is bound to occur above the weld pool as a protective medium during the rapid heating and cooling process (Ref. 34). Hence, retarding the cooling rate of an existing or emerging welding process will require a detailed understanding of bubble configuration in underwater wet welding. This understanding can lead to the improvement of thermal properties in underwater wet welding to mitigate the detrimental effect of bubble configuration on heat losses while exploiting the benefits of bubble-induced phenomena.

In this paper, finite element analysis of the temperature field with consideration of the bubble configuration was carried out in underwater wet welding. As the first step in a series of studies, the key issue for numerical analysis of the temperature field in underwater wet welding is how to involve a bubble configuration that reflects the thermo-physical characteristics of the welding process. The model was validated by comparing the predicted weld profile with measured results. In particular, the heat evolution characteristic and the influences that the equivalent contact radius of the bubble and its floating frequency have on the temperature field were highlighted. The results provide valuable theoretical
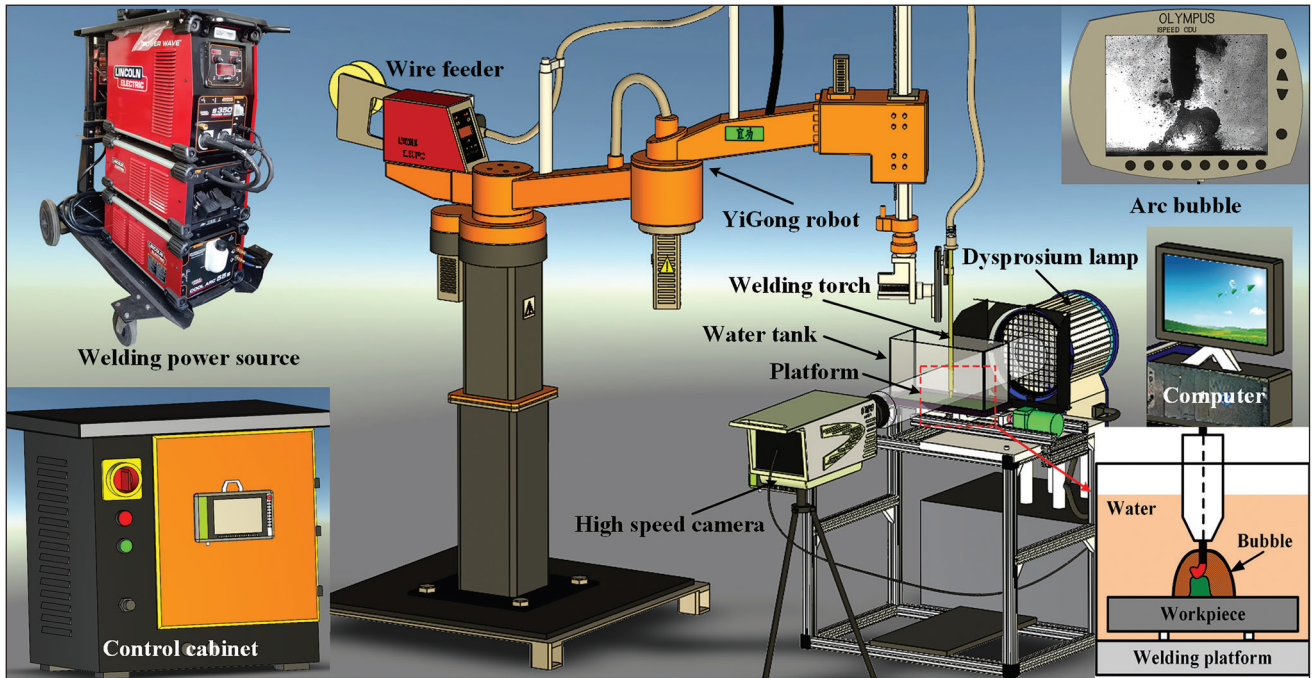
Fig. 2 — Experimental system of underwater wet welding.

Experimental Procedure

Figure 2 shows the schematic illustration of the underwater wet welding system, which mainly consisted of a five-axis robot as well as a control cabinet, a Lincoln Electric Power Wave® S350 welding power source, a platform on which a water tank was provided, and a real-time monitoring system. The base material used in the experiment was rolled E40 ship plate steel with 8 mm thickness, 100 mm length, and 55 mm width. The welding tests were conducted in the butt joint configuration at a water depth of 0.25 m. A 30 deg groove was machined on one side of the steel plate, leaving a 2-mm-thick root surface with no opening between the root surface of the two plates. The chemical composition of the base material (in wt-%) was 0.15% C, 1.06% Mn, 0.25% Si, 0.04% Cr, 0.02% Cu, 0.023% Al, 0.01% Ni, ≤ 0.03% S, 0.013% P, and Fe balance. The consumable wire electrode was CHT81Ni2 with a diameter of 1.2 mm melted under the underwater wet welding conditions. The chemical composition of the wire (in wt-%) was 0.074% C, 1.24% Mn, 0.42% Si, 0.021% Cr, 2.2% Ni, 0.011% P, and Fe balance.

The real-time monitoring system included a welding electrical signal acquisition unit and a high-speed imaging unit. During the welding process, the former was employed to detect and record the waveforms of arc voltage and welding current at a sampling frequency of 10 kHz. The average values of the arc voltage and welding current were then reported. The latter was applied to image the bubble configuration in underwater wet welding using an Olympus i-SPEED 3
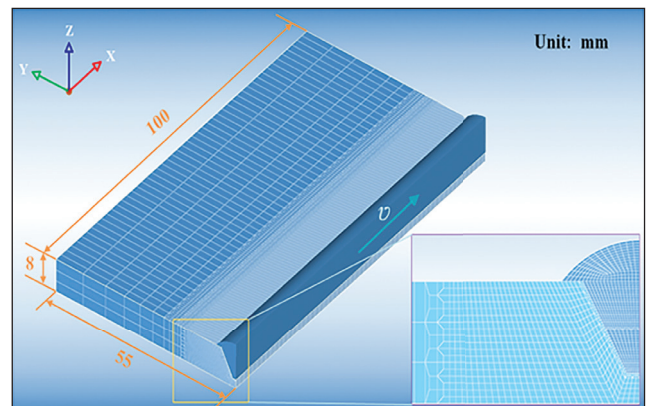
Fig. 3 — Mesh generation of the 3D transient heat transfer model.

high-speed camera with a sampling frequency of 2000 frames/s in conjunction with a dysprosium lamp as a back-light source. Based on the observed video sequence of the bubble, the bubble's geometric features reflecting its physical dynamics were derived in one cycle.

During the welding process shown in Fig. 2, the same process variables were determined by uniform experimental design, and the utilized average welding current was 192 A and the average arc voltage was 32 V. The welding torch was kept stationary, and the welding platform was moved at 2 mm/s. To verify the effectiveness of the finite element model, metallographic specimens were prepared by a wire-cutting machine from the middle position of the weld bead perpendicular to the welding direction.
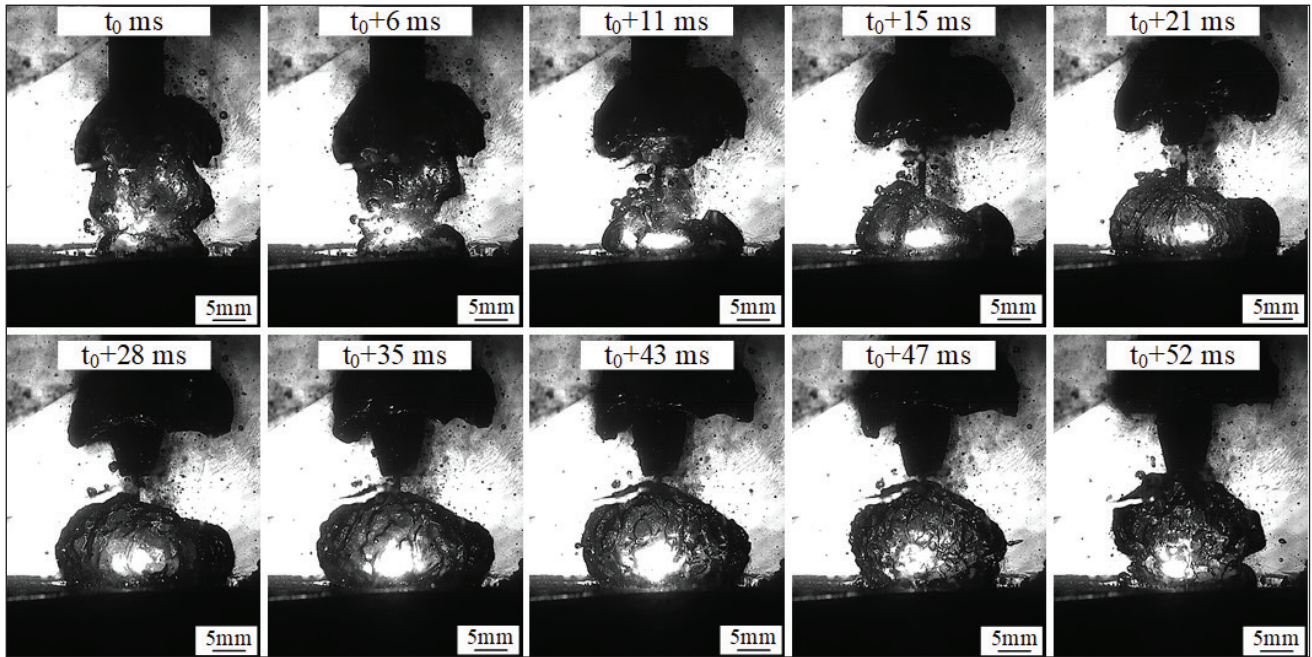
Fig. 4 — Video sequence of the bubble growth process at ten different frames in underwater wet welding.

Numerical Procedure

Geometrical Model

In this work, a 3D transient heat transfer model was developed for thermal analysis of the weld during the underwater wet welding process, and the temperature field was solved by using the finite element method with ANSYS Parametric Design Language (APDL). To achieve an accurate and efficient finite element model, the meshing model was generated in preprocessor hypermesh to ensure meshing quality. Figure 3 shows the finite element meshing model with the same geometrical condition as the experiment. Due to the symmetry of the model, only half of the workpiece was established as the computational domain to save computing time. To better capture the heat evolution process of underwater wet welding, dense meshes of approximately 0.3 mm were used for the weld zone and heat-affected zone, while the grids became coarser for the unaffected base material, as illustrated in Fig. 3. At the same time, the weld reinforcement profile was also analytically estimated to provide the same discretized geometry as the experimental cases in the heat transfer analysis of underwater wet welding. Further, the reinforcement profile can be parabolic by the trial-and-error method (Ref. 16). In total, the number of solid elements and the nodes of the model were 395,850 and 418,737, respectively. With regard to the filling process, the element birth and death technique was essential to involve in the model for ensuring reasonable simulation results. In this technique, all elements in the joint were deactivated by multiplying their stiffness matrix by a very small value prior to triggering the welding process. As the simulation process proceeded, the elements behind the heat source center were activated step by step with the moving of the welding heat source.

Establishment of Bubble Contact Radius

The finite element software ANSYS was adopted in modeling the temperature distribution for underwater wet welding. Constrained by its capability of handling gas, fluid, and solid phases in one simulation model, the software did not directly model the bubble dynamics in the following simulation models. Instead, the effect of the bubble configuration on the model was considered by mathematically modeling the gas-covered interface between the workpiece surface and the bubble (i.e., bubble contact area). As shown in Fig. 4, the actual bubble continued to grow and rise until it broke away from the upper surface of the workpiece, at which time a new bubble started to form on the upper surface of the workpiece. As a result, the bubble evolution process repeated itself again and again. To mathematically predict the bubble-induced phenomena, an idealized bubble-growth process with bubble formation from the workpiece surface was simulated by a semi-empirical method. It was assumed that the bubble dynamics were deemed as an ideal gas behavior and their growth could only begin on the workpiece surface. At the same time, the bubble shape, especially late in its growth, was assumed to be spherical at any time, as shown in Fig. 5.

Figure 6 shows an improved mathematical model of bubble growth and defines the terms of bubble geometry. In this model, the balance of inertial and buoyant forces was considered, while surface tension was always neglected due to the large floating frequency of the bubble. According to Tsai and Masubuchi (Ref. 16), the bubble height at any time can be expressed as the following:

$$h = kt^2 \tag{1}$$

where h is the bubble height, t is the time, and k is the coefficient, which is closely related to bubble dynamics. Specially,
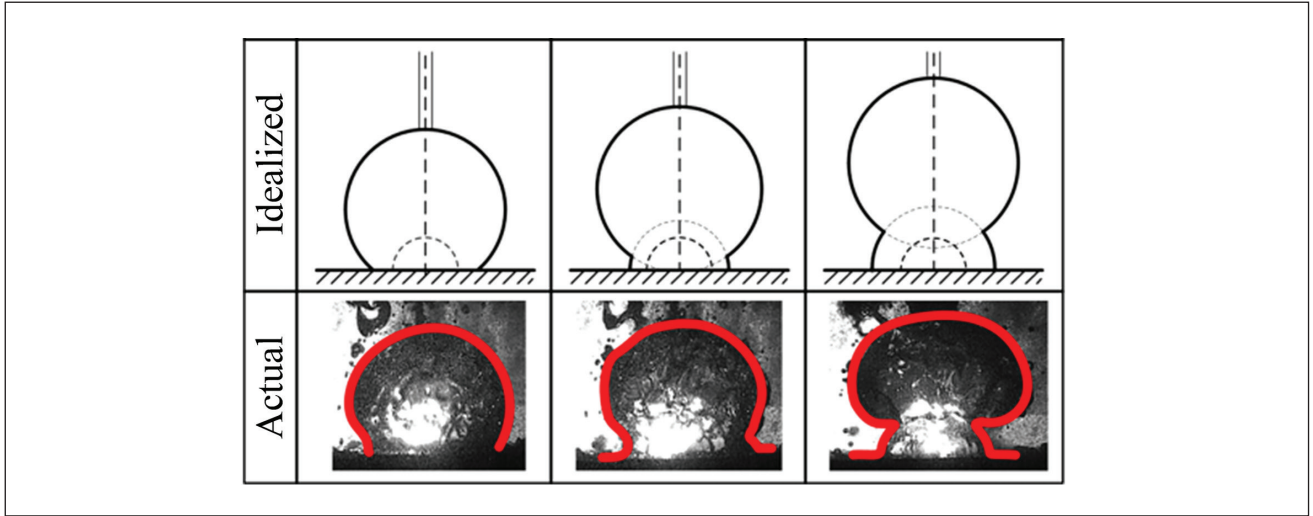
Fig. 5 — Comparison of idealized bubble growth with the actual time of bubble growth in underwater wet welding.

when the bubble departs from the upper surface of the workpiece, a cycle is reached. The height of a departing bubble can be described as the following:

$$h_{max} = kt_{max}^2 \qquad (2)$$

where h_{max} is the height of a departing bubble (i.e., maximum height), and t_{max} is the cycle time, which is inversely proportional to the bubble floating frequency f.

The radius of the gas-covered interface between the workpiece surface and the bubble can be written as the following:

$$R_{c = \sqrt{R^2 - h^2}} \qquad (3)$$

where R_c is the bubble contact radius on the workpiece surface, and R is the bubble radius. It should be noted that the bubble contact radii at the stable bubble ($t = 0$) and departing bubble ($t = t_{max}$) stages were assumed to be the same in this model. Thus, R, h, and R_c values can be given as the following expression using time discretization:

$$\begin{cases} R = R_0, \ h = 0, \ R_c = R_0 & (t = 0) \\ R = R_{max}, \ h = h_{max}, \ R_c = R_0 & (t = t_{max}) \end{cases} \qquad (4)$$

where R_{max} is the maximum bubble radius and R_0 is the radius of the stable bubble on the workpiece surface (i.e., original radius). Further, when $t = t_{max}$, the height of a departing bubble can be also described as:

$$h_{max} = \sqrt{R_{max}^2 - R_0^2} \qquad (5)$$

Therefore, the bubble height at any time can be determined by the solution of Equations 1–5 as the following:

$$h = \sqrt{R_{max}^2 - R_0^2}(ft)^2 \qquad (6)$$

In addition, the bubble radius at any time can be obtained by the solution of Equations 1–6 as the following:

$$R = R_0 + (R_{max} - R_0)(ft)^{\frac{1}{3}} \qquad (7)$$

Based on the above equations, the bubble contact radius R_c can be described as:

$$R_c = \sqrt{\left[R_0 + (R_{max} - R_0)(ft)^{\frac{1}{3}}\right]^2 - \left(R_{max}^2 - R_0^2\right)(ft)^4} \qquad (8)$$

In Equation 8, R_0, R_{max}, and f can be measured by using a high-speed photographic technique during the welding process. According to the used processing variables, the values of R_0, R_{max}, and f were demonstrated to be approximately 5 mm, 12.5 mm, and 20 Hz. The quantitative relationship between R_c and t was then determined by Equation 8.

In underwater wet welding, boundary heat losses can be correlated with the bubble configuration using a semiempirical technique. In this case, the equivalent contact radius of the bubble R_{ce} can be introduced, and the general equation to be solved is the following:

$$R_{ce} = \frac{1}{t_{max}} \int_0^{t_{max}} R_c dt \qquad (9)$$

Figure 7 displays the contact radius of the bubble with time in one cycle based on Equations 8 and 9. It can be seen that the calculated contact radius of the bubble increased first, reaching its maximum in the case of $t = 0.546 \ t_{max}$ and then gradually decreasing. The maximum contact radius R_{cmax} and equivalent contact radius R_{ce} of the bubble were 10.6 and 9.05 mm, respectively. Furthermore, a comparison of
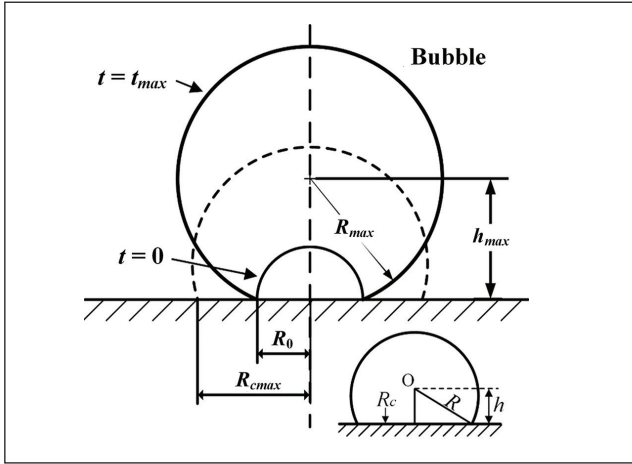
Fig. 6 — The idealized geometric model of bubble growth in underwater wet welding.

Fig. 7 — Contact radius of the bubble with time in one cycle.

high-speed images of in-process bubble contact radius and the theoretical predictions are also presented in Fig. 7. The difference in bubble contact radius between the measured data and the theoretical predictions was rarely observed for every time step, indicating a reasonable representation of the bubble contact area used in the mathematical model representing the effect of the bubble configuration upon the weld pool.

Heat Source Model

This study mainly focused on calculating the temperature distribution of the weld in underwater wet welding by using the 3D heat conduction equation in the transient state with appropriate boundary conditions. The transient heat conduction equation can be given as:

$$\frac{\partial}{\partial x}\left(k\frac{\partial T}{\partial x}\right) + \frac{\partial}{\partial y}\left(k\frac{\partial T}{\partial y}\right) + \frac{\partial}{\partial z}\left(k\frac{\partial T}{\partial z}\right) + q_a = \frac{\partial(\rho C_p T)}{\partial t} \quad (10)$$

where ρ is the density, T is the temperature, C_p is the specific heat, k is the thermal conductivity, t is the time, and q_a is the heat source term.

As illustrated in Fig. 8, a double-ellipsoid heat source proposed by Goldak et al. (Ref. 35) was employed as the heat source model in underwater wet welding. The power density distributions, which describe the front half and the rear half of the heat source, respectively, can be expressed as follows:

$$q_f(x,y,z,t) = \frac{6\sqrt{3}f_f Q}{\pi\sqrt{\pi}a_f bc}\exp\left[-3\frac{(x-\vartheta t-l_0)^2}{a_f^2} -3\frac{y^2}{b^2} -3\frac{z^2}{c^2}\right]$$
$$(x-\vartheta t-l_0) \geq 0 \quad (11)$$
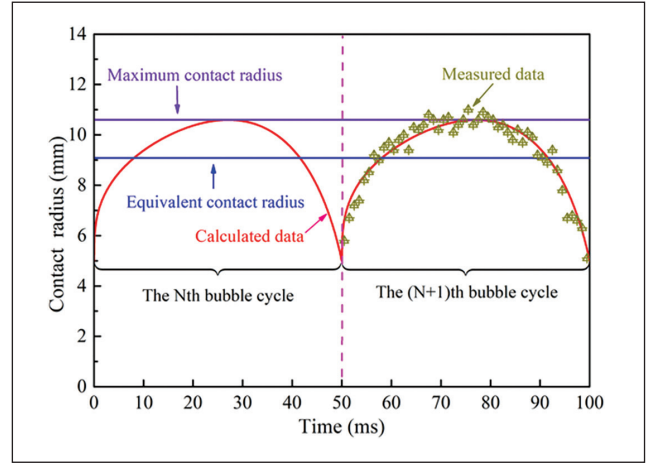
$$q_r(x,y,z,t) = \frac{6\sqrt{3}f_r Q}{\pi\sqrt{\pi}a_r bc}\exp\left[-3\frac{(x-\vartheta t-l_0)^2}{a_r^2} -3\frac{y^2}{b^2} -3\frac{z^2}{c^2}\right]$$
$$(x-\vartheta t-l_0) < 0 \quad (12)$$

$$f_f = \frac{2a_f}{a_f+a_r} \quad (13)$$

$$f_r = \frac{2a_r}{a_f+a_r} \quad (14)$$

where q_f and q_r are the power densities in the front and the rear halves of the arc center, respectively. Q is the effective energy input of the heat source: $Q = \eta UI$, η is the welding heat efficiency whose value was assumed to be 0.65 in our simulation cases, and U and I are the arc voltage and welding current, respectively. l_0 is a position constant where the start point of the welding process is set, and v is the welding speed. a_f and a_r are the lengths of the front and the rear ellipsoid, respectively. b is the half width of the heat source, and c is the depth of the heat source. f_f and f_r are the energy distribution coefficients of the front and rear halves of the heat source, respectively, and $f_f + f_r = 2$ (Ref. 32).

The corresponding distribution parameters of the heat source model were achieved by measuring the geometries of the weld profile. In addition, the determined distribution parameters, such as a_f, a_r, b, and c of the heat source, were slightly modified by running a series of numerical tests so the predicted weld profile could well match the experimental results. In this regard, a_f, a_r, b, and c were assigned the values 5, 10, 9, and 6 mm, respectively. Therefore, $f_f = 0.6$ and $f_r = 1.4$ can be determined by the solutions of Equations 13 and 14.

It should be noted that these distribution parameters were presumed to be the same in the following numerical simulation for comparative purposes even when altering the bubble floating frequency and/or bubble contact radius during the welding process. This is because the contribution of the bubble configuration to the temperature distribution throughout the
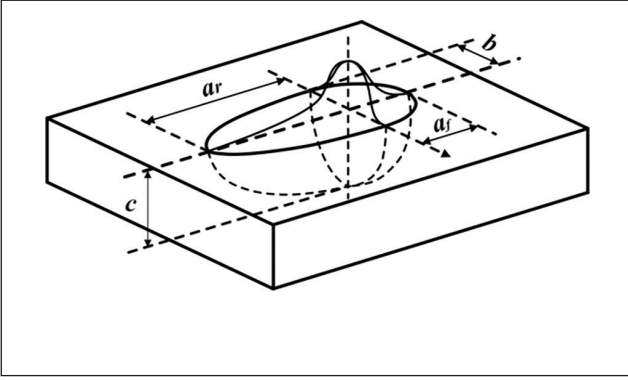
Fig. 8 — Schematic diagram of the double-ellipsoid heat source model.
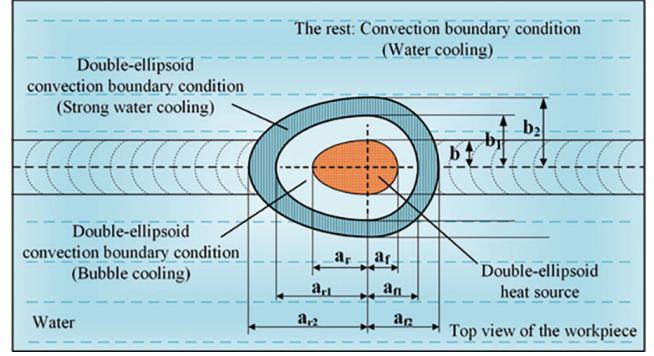
Fig. 9 — Schematic diagram of the thermal convection boundary conditions with consideration of bubble configuration on the upper surface of the workpiece.
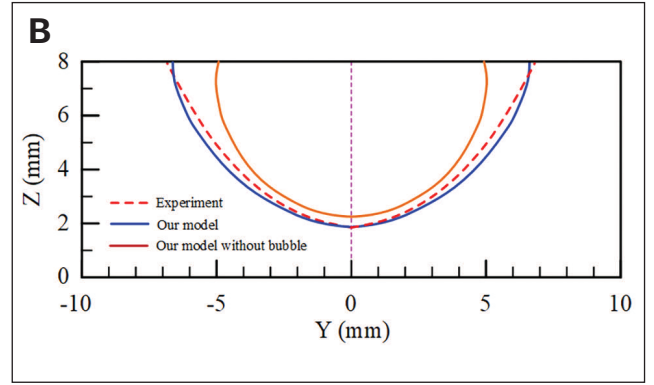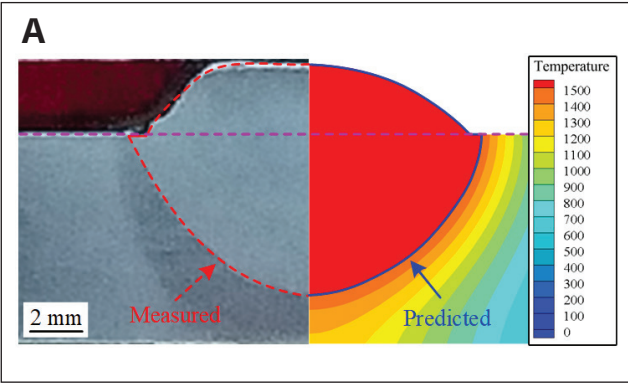
Fig. 10 — Comparisons of numerical and experimental results in underwater wet welding: A — Comparisons of experimentally measured and numerically predicted weld profiles; B — comparisons of the weld profile between the experiment and our model with/without bubble configuration consideration.

model was individually highlighted to account for the bubble-induced physical phenomena in underwater wet welding. On the other hand, incorporating the mathematical model of the bubble contact area into the calculation of the temperature field better captured the effect of the bubble configuration on the weld pool dimensions and other characterized properties of the weld.

Boundary Conditions

The initial condition can be described as the following:

$$T(x,y,z)_{t=0} = T_0 \qquad (15)$$

where T_0 is the ambient temperature, which was assumed to be constant and set to 293 K in this study.

Heat in the weld pool is transferred via heat conduction to the grooved workpiece or solidified weld metal behind the heat source and influences radiation as well as convection effects on the ambient gaseous/water environment. The boundary condition on the upper surface of the workpiece can be expressed as the following:

$$k\frac{\partial T}{\partial n} = q - q_{conv} - q_{rad} \qquad (16)$$

Considering the symmetric model, the adiabatic boundary condition was applied on the symmetric plane of the workpiece ($x = 0$) and can be given as the following:

$$\frac{\partial T}{\partial n} = 0 \qquad (17)$$

The boundary condition on other surfaces of the workpiece can be written as the following:

$$k\frac{\partial T}{\partial n} = -q_{conv} - q_{rad} \qquad (18)$$

The heat losses by convection and radiation have the following expressions as described by Cao et al. (Ref. 36) and Zhao et al. (Ref. 37):
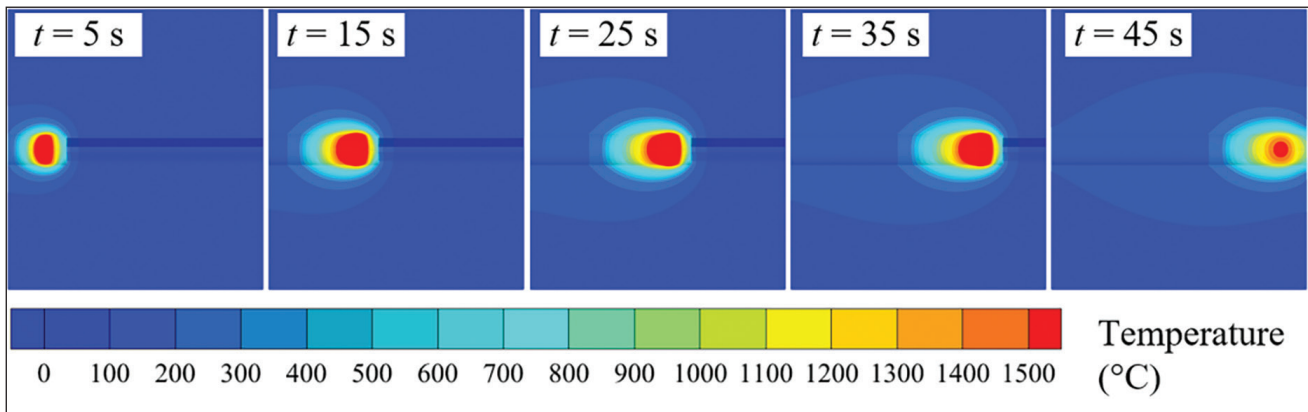
Fig. 11 — Heat distribution of the workpiece surface in underwater wet welding as the heat source is moved along the welding direction.

Table 1 — Thermal Convection Coefficient on the Strong Cooling Area as a Function of the Bubble Floating Frequency

Bubble floating frequency f (Hz)	14	20	26	32	37	42
Convection coefficient h_{conv} (W · m^{-2} · K^{-1})	1500	2500	3500	4500	5500	6500

$$-q_{conv} = h_{conv}(T\text{-}T_0) \tag{19}$$

$$-q_{rad} = \varepsilon_r \sigma_B \left(T^4 \text{-} T_0^4\right) \tag{20}$$

where n is the normal vector of the boundary surface, q is the heat flux on the workpiece surface, q_{conv} is the thermal convection, q_{rad} is the thermal radiation, h_{conv} is the thermal convection coefficient, ε_r is the thermal radiation coefficient whose value was 0.7, and σ_B is the Stefan-Boltzmann constant, which had a value of 5.67×10^{-8} W/(m² · K⁴).

The bubble contact area played a significant role in determining the thermal convection condition and the resulting heat distribution on the workpiece surface. The hot gases and cold water periodically swept this entire area alternatively due to bubble dynamics. The phenomena are very complicated, and a semiempirical method was attempted to explore the order of magnitude of the thermal convection coefficient associated with such bubble growth. In this case, three types of variation in the convection boundary conditions were specifically defined on the workpiece surface, as shown in Fig. 9. Based on the actual configuration of the workpiece surface, the convection boundary layer was divided accordingly into a water cooling area, strong water cooling area, and bubble cooling area. We hypothesize that both the strong water cooling area and the bubble cooling area exhibited similar geometrical parameters to the double-ellipsoid heat source model, and the corresponding geometrical relationship can be expressed as follows:

$$
\begin{aligned}
a_{f1} &= a_f \cdot \frac{b_1}{b} \\
a_{r1} &= a_r \cdot \frac{b_1}{b} \\
a_{f2} &= a_f \cdot \frac{b_2}{b} \\
a_{r2} &= a_r \cdot \frac{b_2}{b}
\end{aligned}
\tag{21}
$$

where a_{f1} and a_{r1} are the lengths of the forward and the rear ellipsoid for the bubble cooling area, respectively; b_1 is the half width of the ellipsoid for the bubble cooling area, which depends substantially on R_{ce} ($b_1 = R^{ce}$); a_{f2} and a_{r2} are the lengths of the forward and the rear ellipsoid for the strong water cooling area, respectively; and b_2 is the half width of the ellipsoid for the strong water cooling area, which is closely related to R_{cmax} and R_{ce} ($b_2 = b_1 + R_{cmax} - R_{ce}$), according to Fig. 9.

Furthermore, the thermal convection coefficient for the water cooling area used in this study can be given according to Pan et al. (Ref. 31) as the following:
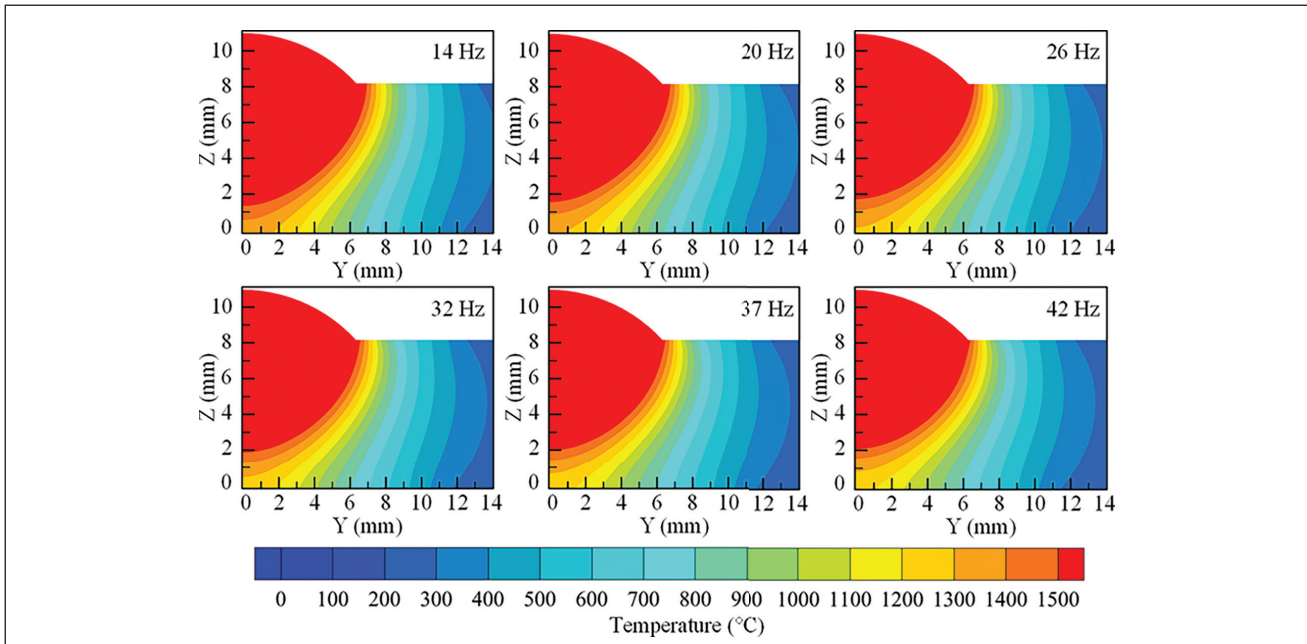
Fig. 12 — Calculated temperature field at the Y-Z transverse cross section as a function of bubble floating frequency.

$$h_{conv} = \begin{cases} 150, & T \leq 373\,K \\ 150+353 \times (T\text{-}100), & 373\,K < T \leq 403\,K \\ 10840\text{-}109 \times (T\text{-}130), & 403\,K < T \leq 493\,K \\ 1030, & 493\,K < T \leq 2273\,K \end{cases} \quad (22)$$

Regarding the bubble cooling area, the temperature inside the bubble was assumed to be uniform, and the thermal convection coefficient was maintained at 25 W/(m² · K) in calculations, which approaches the air cooling conditions for the sake of simplicity.

For the strong water cooling area, forced convection was involved in the boundary conditions, paving a way to incorporate complex agitation of the dynamic bubble above the weld pool surface. Note that the bubble contact radius was varied between R_0 and R_{cmax}. Such a result can very well be because thermal convection transports heat from the workpiece surface into the moving water environment, creating motion by complex agitation of the dynamic bubble. Hence, to maintain consistency in evaluating the role of bubble dynamics, the equivalent contact radius of the bubble R_{ce} was used to define the boundary between the bubble cooling area and the strong water cooling area (i.e., $b_1 = R_{ce}$). Because the bubble periodically floated during the welding process, the effect of the frequency on the forced convection conditions of the strong water cooling area was explored. It was verified that elevating bubble floating frequency tended to trigger more turbulent fluctuations to this area. Accordingly, the heat loss with regard to thermal convection was basically proportional to the water flow field, which is a function of bubble floating frequency, as suggested by Zhao et al. (Ref. 38). Combined with previous cases and experimental results (Refs. 16, 28, 38), the relationship between bubble floating frequency and the forced convection coefficient for the strong water cooling area was reasonably extracted, as displayed in Table 1.

Notably, this variation pattern conformed to our expected results. In this study, we are not concerned with the accuracy of the convection coefficient but instead focused on the effect that the variation in the convection coefficient brought on the temperature field involved in underwater wet welding.

The equivalent contact radius of the bubble remains an informative process parameter in underwater wet welding. Heat losses on the workpiece surface under different equivalent contact radii of the bubble were compared to understand their possible influence on temperature distribution. Making quantitative comparisons among various equivalent contact radii needs to be exercised with caution, especially when probing a broad parameter space. In this case, the equivalent contact radius of the bubble ranged between 6 and 16 mm at 2-mm intervals for comparative purposes while assuming the bubble mathematical model was not affected by the dimensions of the heat source model in underwater wet welding.

Material Properties

The temperature-dependent material thermal properties, including specific heat capacity, thermal conductivity, and density, were taken into consideration in the finite element analysis, as illustrated in Table 2. The base and filler materials were assumed to exhibit the identical thermal properties and to be isotropic. At room temperature, the melting and boiling points were 1773 K and 3272 K, respectively.

Experimental Verification

The established heat transfer model for test cases with a welding current of 192 A, arc voltage of 32 V, and welding speed of 2 mm/s was validated by comparing the predicted weld profile with the experimental results, as shown in Fig. 10. The experimental dotted line and the predicted solid line in

Fig. 10A were drawn along the isotherm of the melting temperature. It can be observed that the predicted weld profile was consistent with the experimental data, which indicates that the thermal representation in the model with consideration of the bubble configuration was reasonably accurate. At the same time, the above results provide key information that the variables used in the finite element model are suitable to predict the key role of the bubble configuration on temperature distribution in underwater wet welding.

To validate the boundary condition modification, the case without considering bubble configuration was further simulated, as displayed in Fig. 10B. It is seen that without considering the bubble configuration, the result is different from that with bubble configuration consideration. Intrinsically, the substitution of water by a gaseous medium is expected to suppress the heat losses by convection. Thus, it was revealed that considerations of the bubble configuration are essential to improve prediction accuracy.
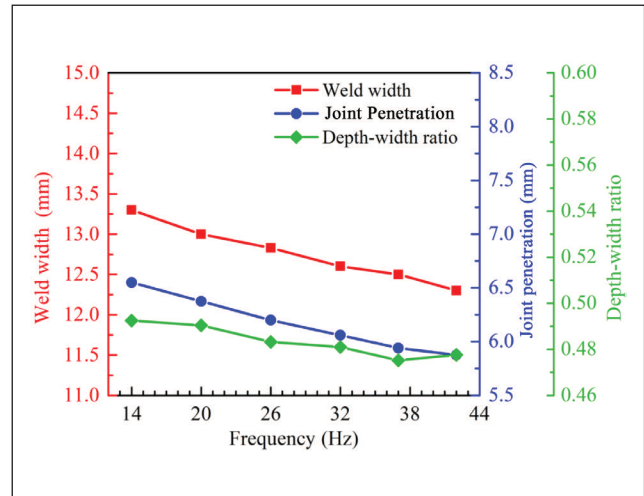
Fig. 13 — Effect of bubble floating frequency on the calculated weld pool dimensions, including weld width, joint penetration, and depth-width ratio.

Table 2 — Temperature-Dependent Thermal Physical Properties of Material

Temperature (K)	Specific Heat (J · kg⁻¹ · K⁻¹)	Thermal Conductivity (W · m⁻¹ · K⁻¹)	Density (kg · m³)
273	430	43.5	7840
293	462	44.6	7840
373	481	43.0	7840
573	530	38.2	7840
673	560	35.7	7840
873	680	30.8	7840
1073	718	25.4	7840
1173	615	26.1	7840
1773	630	33.0	7310
3273	630	33.0	7310
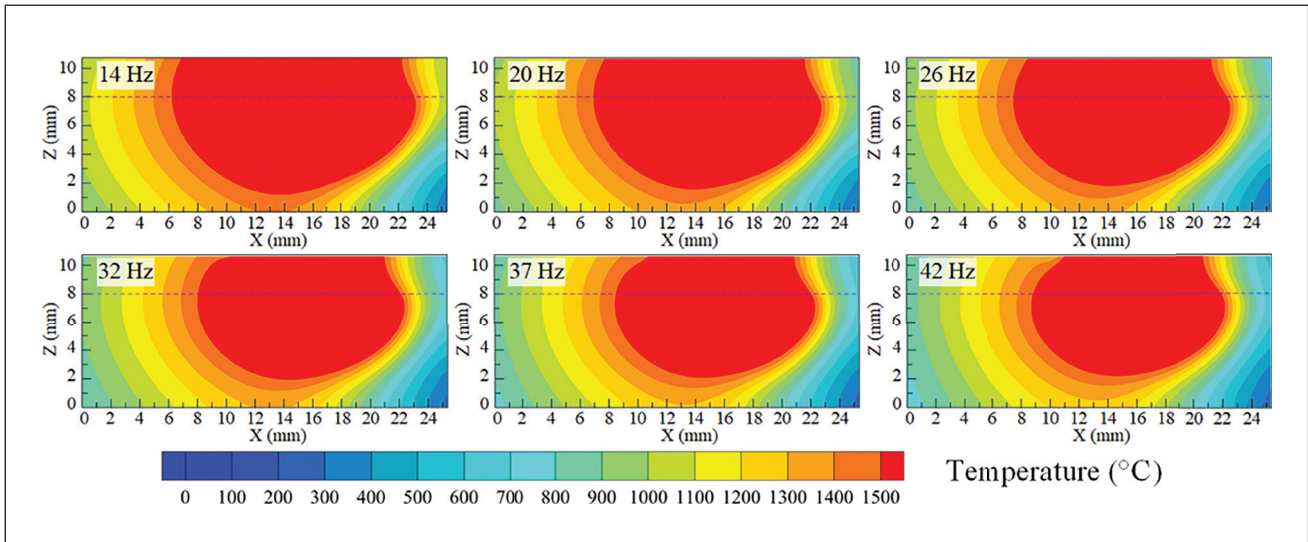
Fig. 14 — Calculated temperature field at the X-Z longitudinal cross section as a function of bubble floating frequency.
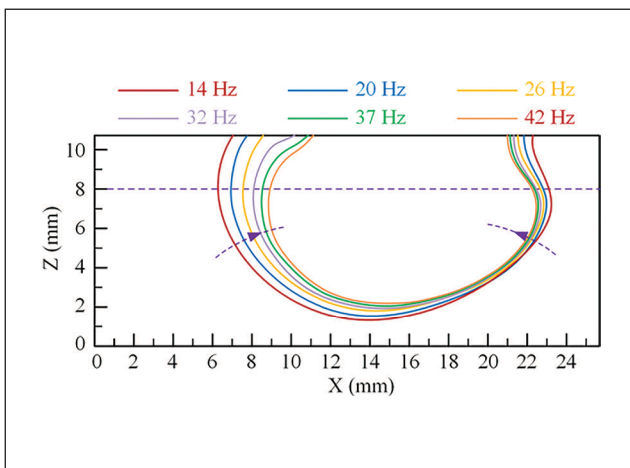
Fig. 15 — Comparison of the weld profile at the X-Z longitudinal cross section as a function of bubble floating frequency.
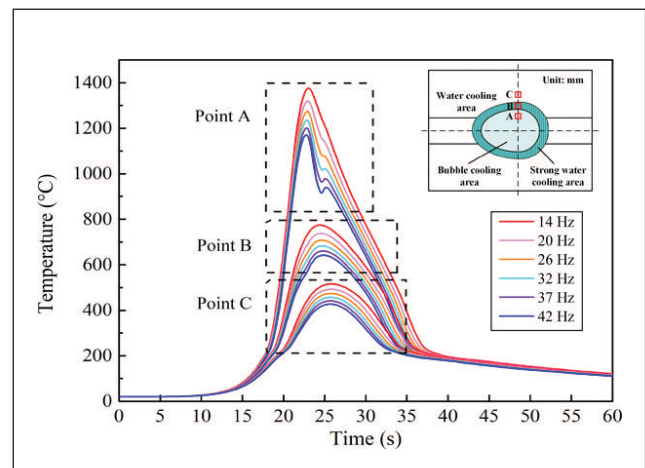
Fig. 16 — Calculated thermal cycles for different bubble floating frequencies at points A, B, and C located on the upper surface of the workpiece.

Results and Discussion

Heat Evolution Process

Figure 11 exhibits the heat evolution process of the workpiece surface in underwater wet welding when the heat source was moved at 5, 15, 25, 35, and 45 s. As the heat source moved forward, the elements behind the heat source center were activated. That is, the welding wire was melted by the heat source to develop into the weld pool. The temperature behind the heat source center decreased gradually as a result of convection and radiation heat transfer to the water environment. Soon after, it dropped below the solidus temperature, and the weld pool started to solidify. Further, the temperature of the workpiece surface was elevated, and the high-temperature area adjacent to the weld pool was invariably enlarged with the ongoing welding process. The heat on the workpiece surface greatly concentrated on the rear half of the heat source. Except for the final moment at 45 s, as the welding process proceeded, the high-temperature area in the weld pool expanded, resulting in a significant trailing of the weld pool tail. Meanwhile, at the beginning of the welding process, only a minor weld pool was produced, and its shape was also very special due to insufficient heat accumulation.

Influence of Bubble Floating Frequency

The temperature field in underwater wet welding was calculated for different bubble floating frequencies based on the material's thermal properties and the modified boundary conditions. Figure 12 shows the effect of bubble floating frequency on the predicted temperature field in the Y-Z plane. Analysis of weld pool shape indicated no significant difference regardless of bubble floating frequency. However, the weld pool dimensions as a function of bubble floating frequency
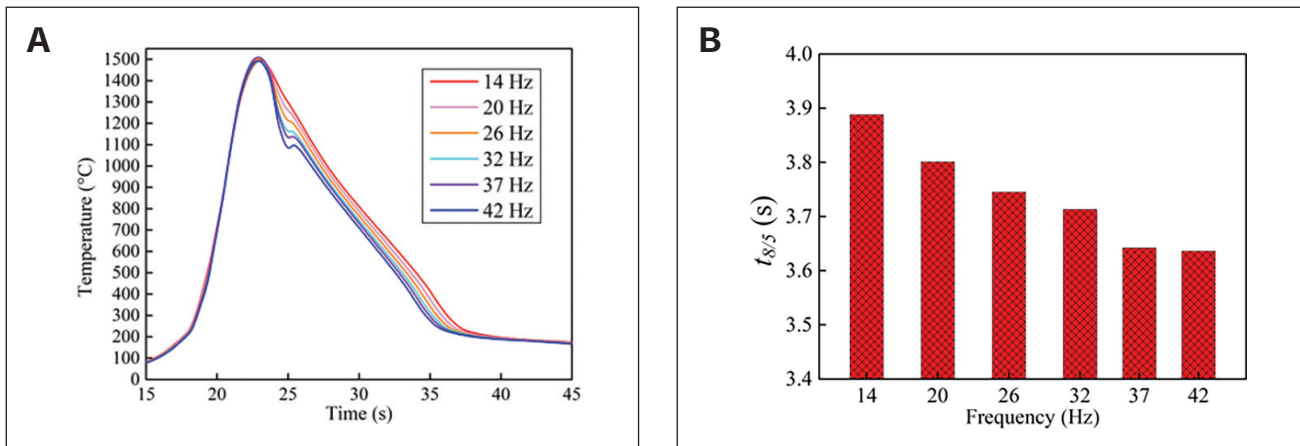
Fig. 17 — Calculated thermal cycle curves at the weld interface (A) and the corresponding $t_{8/5}$ time (B) as a function of bubble floating frequency.
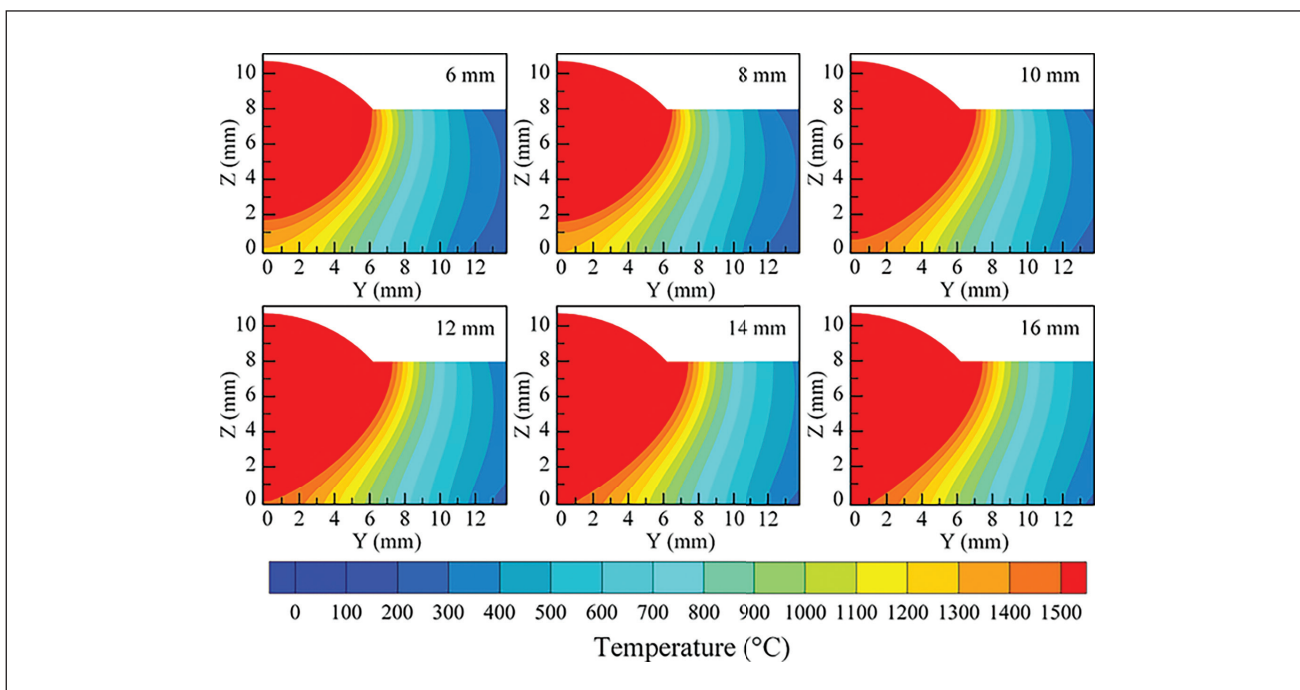
Fig. 18 — Calculated temperature field at the Y-Z transverse cross section as a function of the equivalent contact radius of the bubble.

exhibited a trend of observable differences, implying variations in the dynamic bubble-induced effect. The weld pool dimensions with various bubble floating frequencies were compared to account for the boundary heat loss mechanism brought on by the bubble configuration. The extracted joint penetration, weld width, and depth-width ratio are plotted in Fig. 13. Apparently, a general trend is that joint penetration, weld width, and depth-width ratio all decrease monotonically with the enhancement of bubble floating frequency (i.e., there is more significant heat loss to the water environment with a higher level of floating frequency). A linear correlation is also achieved between weld pool dimension and bubble floating frequency. As the bubble floating frequency increased, reducing the depth-width ratio manifested that the decrement of joint penetration showed a much larger value

than that of the weld width. For example, the decrement was 10.3% for joint penetration and 7.5% for weld width when the frequency increased from 14 to 42 Hz under otherwise identical conditions.

Figure 14 shows the effect of bubble floating frequency on the predicted temperature field in the X-Z plane. And the corresponding weld pool profile is derived in Fig. 15. It can be observed that for any radial direction, the weld pool profile presented a state of contraction from the outside to the inside with increasing bubble floating frequency. Nevertheless, the contraction degree of the weld pool profile in the front half of the heat source was less conspicuous than that in the rear half of the heat source. This is because a better heat conduction condition is present in the front half of the heat source so that the contribution of heat flux to this

area is evidently minimized. However, a stable weld pool had already emerged in the rear half of the heat source, ensuring enough heat accumulation. Consequently, the rear half of the heat source exhibited a larger weld pool dimension than the front half position of the heat source. After the heat source was moved away, a relatively large high-temperature area in the rear half position of the heat source was prone to heat losses to the water environment; in addition, increasing the floating frequency progressively promoted the excessive boundary heat losses under these conditions, thereby leading to a remarkable variation of the weld pool dimension in the rear half of the heat source.

To identify the thermal characteristic of the weld, the thermal cycle of each node in the heat source model was extracted via the simulation postprocessing files. Three representative points, defined as points A, B, and C, distributed in the bubble cooling area, strong water cooling area, and water cooling area, respectively, were emphasized. Figure 16 shows the typical thermal cycle curves of the three points on

Fig. 19 — Effect of the equivalent contact radius of the bubble on the calculated weld pool dimensions including weld width, joint penetration, and depth-width ratio.

the workpiece surface. Each curve presents a bell-shaped distribution characteristic, the width of which is reduced as bubble floating frequency increases. For any given point, the peak temperature generally shows a decreasing trend, and the cooling rate increases with the increase of bubble floating frequency. Under the same frequency, a higher peak temperature value was easily detected in point A followed by point B and then point C. It is also demonstrated in Fig. 16 that the modification of boundary heat loss conditions explaining bubble physical phenomena is adequate for the heat source model and turns out to be reasonable.

Moreover, there is a perturbation for the cooling stage of point A in the case of higher frequency but not at points B and C. This observation correlates well with the fact that dynamic bubble-induced heat losses require a strong water cooling area to define the boundary condition. When point A reached the peak temperature, it was located inside the bubble and always protected in the bubble cooling area. As the heat source moved away from point A, point A passed through a bubble cooling area, strong water cooling area, and water cooling area in sequence and was exposed to these three areas for a period of time. The major difference in the thermal convection condition among these three areas has been observed to modulate the order of magnitude of the heat losses, which may fundamentally be the dominant cause of perturbation.

For in-service welding, the value of $t_{8/5}$ is an important process parameter of the thermal cycle. Figure 17 shows the effect of bubble floating frequency on the calculated thermal cycle curves of the weld interface at the bottom of the weld and the corresponding $t_{8/5}$ time. From Fig. 17A, we notice that the peak temperature at this position was basically the same (i.e., identical melting temperature of the material), and the cooling rate as a function of bubble floating frequency yielded a significant difference under otherwise identical conditions. The extracted $t_{8/5}$ value plotted in Fig. 17B indicates that the variation trend of $t_{8/5}$ generally agrees with that in the weld pool dimensions shown in Fig. 13 when elevating bubble floating frequency, largely owing to acceleration of heat losses in the case of higher frequency. The $t_{8/5}$ value tended to decrease with increasing bubble floating frequency from 14 to 42 Hz.
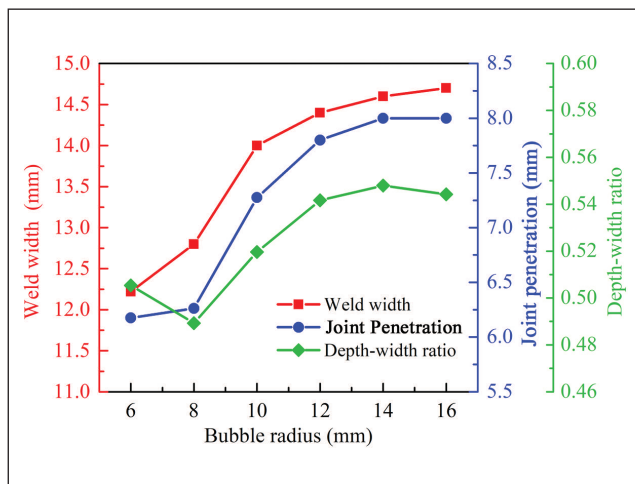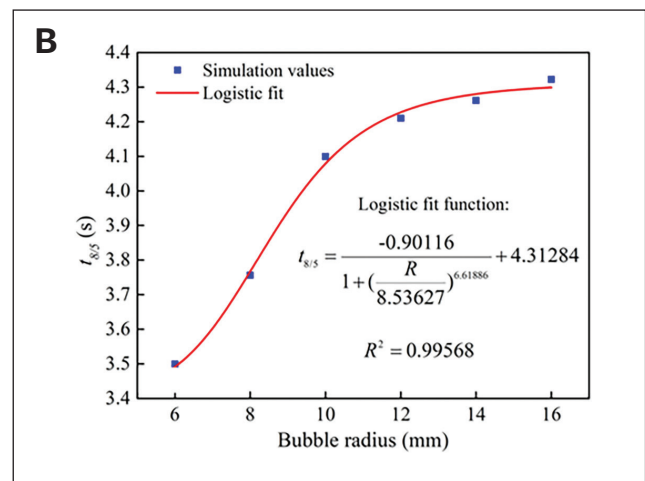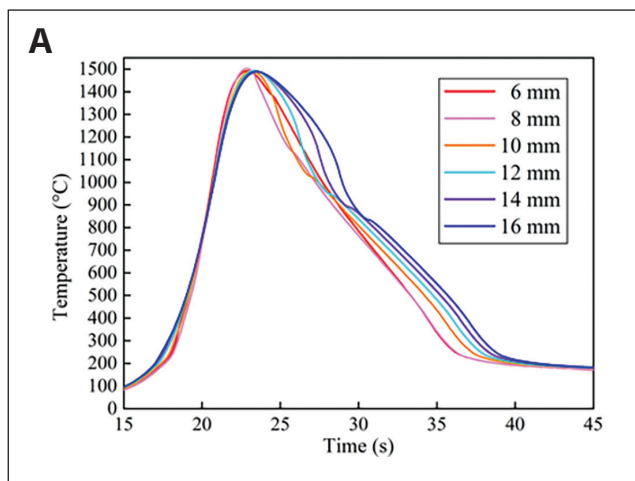
Fig. 20 — Calculated thermal cycle curves at the weld interface (A) and the corresponding $t_{8/5}$ time (B) as a function of the equivalent contact radius of the bubble.

These results imply that reducing the bubble floating frequency opens a new pathway to optimize the temperature distribution in underwater wet welding without changing the processing variables, which is essentially due to the alleviation of bubble disturbance that can effectively compensate for the heat losses in thermal systems.

Influence of the Equivalent Contact Radius of the Bubble

In addition to bubble floating frequency, the variation in the equivalent contact radius of the bubble was also involved in the heat source model. Figure 18 shows the predicted temperature field in the *Y-Z* plane as a function of the equivalent contact radius of the bubble. Similar to the case of bubble floating frequency, no visible difference in weld pool shape was observed along the equivalent contact radius of the bubble. The extracted weld pool dimensions, including joint penetration, weld width, and depth-width ratio, are described in Fig. 19. As the equivalent contact radius of the bubble increased, the weld width continued to increase, while the joint penetration increased sharply and then remained relatively flat. Most significantly, a complete joint penetration weld was observed when the equivalent contact radius of the bubble reached 14 and 16 mm since the larger bubble protection area led to reduced heat loss. Meanwhile, except for the equivalent contact radius of 8 mm, there was a remarkable increase in the depth-width ratio up to a maximum value of 14 mm followed by a slight decrease. Such decrease of depth-width ratio was probably due to the occurrence of a complete joint penetration weld under such conditions. Together, these results show that the increased equivalent contact radius of the bubble attached to the workpiece surface can attenuate the convection heat losses, contributing to an enhanced joint penetration.

In addition, the increment was 29.6% for joint penetration and 20.3% for weld width when the equivalent contact radius varied from 6 to 16 mm. By comparing Fig. 13 with Fig. 19, the variation trend in joint penetration and weld width per unit for the equivalent contact radius of the bubble was more significant than that for the bubble floating frequency. Hence, the equivalent contact radius of the bubble is predicted to exhibit a more significant impact on weld pool dimensions than the bubble floating frequency under the same processing variables.

Figure 20A shows the effect of the equivalent contact radius of the bubble on the predicated thermal cycle curves of the weld interface at the bottom of the weld. For all equivalent contact radii, a similar peak temperature at this position was present. Also, an outstanding feature concerns the depression of the cooling rate when the equivalent contact radius increased from 6 to 12 mm. The corresponding $t_{8/5}$ value was observed for all equivalent contact radii from an examination of Fig. 20B. The $t_{8/5}$ value presented an upward trend with the increasing equivalent contact radius. The changing trend of the $t_{8/5}$ value operated at the small radii was more significant than that at the large radii as the increasing equivalent radius contributed less to heat losses, stemming from increased distance between the heat source and water at the large radii. Meanwhile, a nonlinear fitting equation, inserted in Fig.

20B, can be attained to explain the relationship between the $t_{8/5}$ value and the equivalent contact radius. These results indicate that the increasing level of the equivalent radius provides another effective route to modulating the temperature distribution in underwater wet welding under the same processing variables, which is expected as large-sized bubbles tend to consolidate the protection of the welding zone and enable more heat absorption and heat transfer.

Overall, temperature field evolution can be controlled by manipulating the equivalent contact radius of the bubble and its floating frequency. Hence, with the purpose of obtaining a sound weld under water, one of the primary concerns is to appropriately match the boundary heat loss conditions. To leverage such technology, understanding the complex role of bubble dynamics involved in underwater wet welding is essential. However, it was revealed by Wang et al. (Ref. 21) and Li et al. (Ref. 39) that the control of bubble dynamics is governed by the level of heat input, which is determined by processing variables from underwater wet welding. Also, the level of heat input is directly related to the cooling rate during welding and also to the weld pool dimensions (Ref. 40). Thus, it is a complicated issue to harness the synergies between bubble configuration and heat input to realize the simultaneous optimization of bubble-induced heat losses and weld performance.

To decouple the contributions of the bubble configuration and heat input to a temperature field associated with the cooling rate in underwater wet welding, the active control of the bubble configuration is critical and enabled by the superior combination of careful processing variables and specific extra energy additions. First, the former can be designed and optimized to maintain arc consistency, promote metal transfer, and achieve a defect-free weld (Refs. 41, 42); and second, the latter can involve several online process modifications, such as a mechanical constraint system (Ref. 43), an ultrasonic vibration technique (Refs. 44, 45), and the submerged arc method assisted by an organic adhesive (Ref. 46). With all this in mind, such a combined approach would allow for a more thoughtful and efficient method to engineer a high-performance weld joint while tuning the bubble configuration and then altering the heat loss conditions.

Conclusions

In this paper, a heat source model was established to simulate the temperature field in underwater wet welding. To improve the prediction accuracy of the model, boundary conditions took the contribution of the bubble configuration into account. The roles of the equivalent contact radius of the bubble and bubble floating frequency on the weld pool dimensions and thermal cycles were investigated in detail. The weld profile predicted by numerical simulation was consistent with the experimental results. The main conclusions are summarized as follows:

1) A semiempirical method that divides the convection boundary layer on the workpiece surface into the water cooling area, strong water cooling area, and bubble cooling area was proposed in this study. It was proven to be able to elaborate both the contribution of the bubble configuration and the associated heat loss mechanism.

2) Bubble dynamics play a critical role in temperature distribution and are primarily governed by thermal convection conditions. Differences in the convection coefficient between gaseous and water environments tend to affect weld pool dimensions and thermal cycles but allow a similar weld pool shape.

3) Low bubble floating frequency and/or high equivalent contact radius of the bubble yield the depression of heat losses to the water environment and thus induce an increase in weld width and joint penetration. By comparison, the contribution of the equivalent contact radius of the bubble dominates.

4) Suggestions regarding the matching strategy of bubble configuration and heat input for underwater wet welding may be provided. The addition of an online process modification method with controlled bubble configuration is recommended to match the optimized processing variables, thereby delivering a high-performance weld joint and consolidating our understanding of bubble-induced phenomena.

References

1. Swierczyńska, A., Fydrych, D., and Rogalski, G. 2017. Diffusible hydrogen management in underwater wet self-shielded flux cored arc welding. *International Journal of Hydrogen Energy* 42(38): 24532–24540. DOI: 10.1016/j.ijhydene.2017.07.225

2. Colak, Z., Ayan, Y., and Kahraman, N. 2020. Weld morphology and mechanical performance of marine structural steel welded underwater in a real marine environment. *The International Journal of Advanced Manufacturing Technology* 109(1–2): 491–501. DOI: 10.1007/s00170-020-05679-y

3. Menezes, P. H. R., Pessoa, E. C. P., and Bracarense, A. Q. 2019. Comparison of underwater wet welding performed with silicate and polymer agglomerated electrodes. *Journal of Materials Processing Technology* 266: 63–72. DOI: 10.1016/j.jmatprotec.2018.10.019

4. Parshin, S. G., Levchenko, A. M., and Maystro, A. S. 2020. Metallurgical model of diffusible hydrogen and non-metallic slag inclusions in underwater wet welding of high-strength steel. *Metals* 10(11): 1498. DOI: 10.3390/met10111498

5. Oliveira, F. D. R., Soares, W. R., and Bracarense, A. Q. 2014. Study correlating the bubble phenomenon and electrical signals in underwater wet welding with covered electrodes. *Welding International* 29(5): 363–371. DOI: 10.1080/09507116.2014.932980

6. Wang, J., Sun, Q., Ma, J., Teng, J., Jin, P., and Feng, J. 2019. Investigation of acoustic radiator affecting bubble-acoustic interaction in ultrasonic wave-assisted UWW at shallow water. *Journal of Manufacturing Processes* 37: 563–577. DOI: 10.1016/j.jmapro.2018.12.020

7. Bari, S. D., and Robinson, A. J. 2014. Experimental study of gas injected bubble growth from submerged orifices. *Experimental Thermal and Fluid Science* 44: 124–137. DOI: 10.1016/j.expthermflusci.2012.06.005

8. Jia, C. B., Zhang, Y., Zhao, B., Hu, J. K., and Wu, C. S. 2016. Visual sensing of the physical process during underwater wet FCAW. *Welding Journal* 95(6): 202-s to 209-s.

9. Jia, C. B., Wu, J., Han, Y., Zhang, Y., Yang, Q., and Wu, C. S. 2020. Underwater pulse-current FCAW — Part 1: Waveform and process features. *Welding Journal* 99(6): 135-s to 145-s. DOI: 10.29391/2020.99.013

10. Feng, J., Wang, J., Sun, Q., Zhao, H., Wu, L., and Xu, P. 2017. Investigation on dynamic behaviors of bubble evolution in underwater wet flux-cored arc welding. *Journal of Manufacturing Processes* 28: 156–167. DOI: 10.1016/j.jmapro.2017.06.003

11. Wang, J., Sun, Q., Zhang, T., Tao, X., Jin, P., and Feng, J. 2019. Arc stability indexes evaluation of ultrasonic wave-assisted underwater FCAW using electrical signal analysis. *The International Journal of Advanced Manufacturing Technology* 103(5–8): 2593–2608. DOI: 10.1007/s00170-019-03463-1

12. Chen, H., Guo, N., Huang, L., Zhang, X., Feng, J., and Wang, G. 2019. Effects of arc bubble behaviors and characteristics on droplet transfer in underwater wet welding using in-situ imaging method. *Materials & Design* 170: 107696. DOI: 10.1016/j.matdes.2019.107696

13. Chen, H., Guo, N., Shi, X., Du, Y., Feng, J., and Wang, G. 2018. Effect of hydrostatic pressure on protective bubble characteristic and weld quality in underwater flux-cored wire wet welding. *Journal of Materials Processing Technology* 259: 159–168. DOI: 10.1016/j.jmatprotec.2018.04.037

14. Wang, J., Sun, Q., Pan, Z., Yang, J., and Feng, J. 2019. Effects of welding speed on bubble dynamics and process stability in mechanical constraint-assisted underwater wet welding of steel sheets. *Journal of Materials Processing Technology* 264: 389–401. DOI: 10.1016/j.jmatprotec.2018.09.022

15. Chen, H., Guo, N., Shi, X., Du, Y., Feng, J., and Wang, G. 2018. Effect of water flow on the arc stability and metal transfer in underwater flux-cored wet welding. *Journal of Manufacturing Processes* 31: 103–115. DOI: 10.1016/j.jmapro.2017.11.010

16. Tsai, C. L., and Masubuchi, K. 1979. Mechanisms of rapid cooling in underwater welding. *Applied Ocean Research* 1(2): 99–110. DOI: 10.1016/0141-1187(79)90023-3

17. Arias, A. R., and Bracarense, A. Q. 2017. Fatigue crack growth assessment in underwater wet welds. *Welding Journal* 96(8): 287-s to 294-s.

18. Klett, J., Hecht-Linowitzki, V., Grünzel, O., Schmidt, E., Maier, H. J., and Hassel, T. 2020. Effect of the water depth on the hydrogen content in SMAW wet welded joints. *SN Applied Sciences* 2: 1269. DOI: 10.1007/s42452-020-3066-8

19. Tomków, J., and Janeczek, A. 2020. Underwater in situ local heat treatment by additional stitches for improving the weldability of steel. *Applied Sciences* 10(5): 1823. DOI: 10.3390/app10051823

20. Tomków, J., Rogalski, G., Fydrych, D., and Babanowski, J. 2018. Improvement of S355G10+N steel weldability in water environment by temper bead welding. *Journal of Materials Processing Technology* 262: 372–381. DOI: 10.1016/j.jmatprotec.2018.06.034

21. Wang, J., Sun, Q., Hou, S., Zhang, T., Jin, P., and Feng, J. 2019. Dynamic control of current and voltage waveforms and droplet transfer for ultrasonic-wave-assisted underwater wet welding. *Materials & Design* 181: 108051. DOI: 10.1016/j.matdes.2019.108051

22. Yang, Q., Han, Y., Jia, C., Wu, J., Dong, S., and Wu, C. 2019. Impeding effect of bubbles on metal transfer in underwater wet FCAW. *Journal of Manufacturing Processes* 45: 682–689. DOI: 10.1016/j.jmapro.2019.08.013

23. Jia, C., Zhang, Y., Wu, J., Xing, C., Zhao, B., and Wu, C. 2019. Comprehensive analysis of spatter loss in wet FCAW considering interactions of bubbles, droplets and arc — Part 1: Measurement and improvement. *Journal of Manufacturing Processes* 40: 122–127. DOI: 10.1016/j.jmapro.2019.03.013

24. Xing, C., Jia, C., Han, Y., Dong, S., Yang, J., and Wu, C. 2020. Numerical analysis of the metal transfer and welding arc behaviors in underwater flux-cored arc welding. *International Journal of Heat and Mass Transfer* 153: 119570. DOI: 10.1016/j.ijheatmasstransfer.2020.119570

25. Wang, J., Sun, Q., Zhang, S., Wang, C., Wu, L., and Feng, J. 2018. Characterization of the underwater welding arc bubble through a visual sensing method. *Journal of Materials Processing Technology* 251: 95–108. DOI: 10.1016/j.jmatprotec.2017.08.019

26. Zhao, B., Chen, J., Wu, C., and Shi, L. 2020. Numerical simulation of bubble and arc dynamics during underwater wet flux-cored arc welding. *Journal of Manufacturing Processes* 59: 167–185. DOI: 10.1016/j.jmapro.2020.09.054

27. Vafaei, S., Angeli, P., and Wen, D. Bubble growth rate from stainless steel substrate and needle nozzles. *Colloids and Surfaces A: Physicochemical and Engineering Aspects* 384(1): 240–247. DOI: 10.1016/j.colsurfa.2011.03.066

28. Zhao, B., Chen, J., Jia, C., and Wu, C. 2018. Numerical analysis of molten pool behavior during underwater wet FCAW process. *Journal of Manufacturing Processes* 32: 538–552. DOI: 10.1016/j.jmapro.2018.03.020

29. Ronda, J., Mahrenholtz, O., and Hamann, R. 1992. Thermomechanical simulation of underwater welding processes. *Archive of Applied Mechanics* 62: 15–27. DOI: 10.1007/BF00786678

30. Ghadimi, P., Ghassemi, H., Ghassabzadeh, M., and Kiaei, Z. 2013. Three-dimensional simulation of underwater welding and investigation of effective parameters. *Welding Journal* 92(12): 239-s to 249-s.

31. Pan, J., Yang, L., Hu, S., and Chai, S. 2015. Numerical analysis of thermal cycle characteristics and prediction of microstructure in multi-pass UWW. *The International Journal of Advanced Manufacturing Technology* 84(5–8): 1095–1102. DOI: 10.1007/s00170-015-7787-6

32. Wang, J., Shi, J., Wang, J., Li, W., Liu, C., Xu, G., Maksimov, S. Y., and Zhu, Q. 2017. Numerical study on the temperature field of underwater flux-cored wire arc cutting process. *The International Journal of Advanced Manufacturing Technology* 91(5–8): 2777–2786. DOI: 10.1007/s00170-016-9913-5

33. Tsai, C. L., Yao, P. L., and Hong, J. K. 1997. Finite element analysis of underwater welding repairs. *Welding Journal* 76(8): 283-s to 288-s.

34. Wang, J., Sun, Q., Zhang, T., Xu, P., and Feng, J. 2019. Experimental study of arc bubble growth and detachment from underwater wet FCAW. *Welding in the World* 63(6): 1747–1759. DOI: 10.1007/s40194-019-00776-3

35. Goldak, J., Chakravarti, A., and Bibby, M. 1984. A new finite element model for welding heat sources. *Metallurgical Transactions B* 15(2): 299–305. DOI: 10.1007/BF02667333

36. Cao, Y., Lin, X., Kang, N., Ma, L., Wei, L., Zheng, M., Yu, J., Peng, D., and Huang, W. 2021. A novel high-efficient finite element analysis method of powder bed fusion additive manufacturing. *Additive Manufacturing* 46: 102187. DOI: 10.1016/j.addma.2021.102187

37. Zhao, B., Wu, C., Jia, C., and Yuan, X. 2013. Numerical analysis of the weld bead profiles in underwater wet flux-cored arc welding. *Acta Metallurgica Sinica* 49(7): 797–803. DOI: 10.3724/SP.J.1037.2013.00061

38. Zhao, B., Wu, C., Jia, C., and Yuan, X. 2013. Numerical simulation of influence of water depth and flowing speed on thermal process of underwater wet welding. *Transactions of the China Welding Institution* 34(08): 55–58.

39. Li, H., Liu, D., Yan, Y., Guo, N., Liu, Y., and Feng, J. 2018. Effects of heat input on arc stability and weld quality in underwater wet flux-cored arc welding of E40 steel. *Journal of Manufacturing Processes* 31: 833–843. DOI: 10.1016/j.jmapro.2018.01.013

40. Di, X., Ji, S., Cheng, F., Wang, D., and Cao, J. 2015. Effect of cooling rate on microstructure, inclusions and mechanical properties of weld metal in simulated local dry underwater welding. *Materials & Design* 88: 505–513. DOI: 10.1016/j.matdes.2015.09.025

41. Omajene, J. E., Martikainen, J., Wu, H., and Kah, P. 2014. Optimization of underwater wet welding process parameters using neural network. *International Journal of Mechanical and Materials Engineering* 9: 26. DOI: 10.1186/s40712-014-0026-3

42. Pessoa, E. C. P., and Liu, S. 2021. The state of the art of underwater wet welding practice: Part 2. *Welding Journal* 100(5): 171-s to 182-s. DOI: 10.29391/2021.100.014

43. Wang, J., Sun, Q., Jiang, Y., Zhang, T., Ma, J., and Feng, J. 2018. Analysis and improvement of underwater wet welding process stability with static mechanical constraint support. *Journal of Manufacturing Processes* 34: 238–250. DOI: 10.1016/j.jmapro.2018.06.007

44. Wang, J., Sun, Q., Teng, J., and Feng, J. 2019. Bubble evolution in ultrasonic wave-assisted underwater wet FCAW. *Welding Journal* 98(5): 150-s to 163-s. DOI: 10.29391/2019.98.012

45. Wang, J., Liu, Y., Feng, J., and Sun, Q. 2021. Microstructure evolution of E40 steel weldments in ultrasonic-wave-assisted underwater FCAW. *Welding Journal* 100(3): 106-s to 120-s. DOI: 10.29391/2021.100.009

46. Dong, S., Han, Y., Jia, C., Wu, C., Zhang, M., Yang, Q., and Yang, J. 2020. Organic adhesive assisted underwater submerged-arc welding. *Journal of Materials Processing Technology* 284: 116739. DOI: 10.1016/j.jmatprotec.2020.116739

JIANFENG WANG is with the College of Materials Science and Technology, Nanjing University of Aeronautics, Nanjing, China, and with the School of Metallurgy, Northeastern University, Shenyang, China. **YUYING CHEN** (*chenyy@ral.neu.edu.cn*) is with State Key Laboratory of Rolling and Automation, Northeastern University, Shenyang, China. **JINPING LIU** is with Key Laboratory for Highly Efficient and Intelligent Welding of China National Nuclear Corp., China Nuclear Industry 23 Construction Co. Ltd., Beijing, China. **TAO ZHANG** is with Institute for Materials Research, Tohoku University, Japan. **CHENG LIU, CANCAN YAN,** and **YINGCHAO FENG** (*fengcni23@163.com*) are also with Key Laboratory for Highly Efficient and Intelligent Welding of China National Nuclear Corp., China Nuclear Industry 23 Construction Co. Ltd., Beijing, China.